

LEARNING UNIFIED REPRESENTATION OF 3D GAUSSIAN SPLATTING

Yuelin Xin^{1*} Yuheng Liu¹ Xiaohui Xie¹ Xinke Li^{2,†}

¹UC Irvine ²City University of Hong Kong

ABSTRACT

A well-designed vectorized representation is crucial for the learning systems natively based on 3D Gaussian Splatting. While 3DGS enables efficient and explicit 3D reconstruction, its parameter-based representation remains hard to learn as features, especially for neural-network-based models. Directly feeding raw Gaussian parameters into learning frameworks fails to address the non-unique and heterogeneous nature of the Gaussian parameterization, yielding highly data-dependent models. This challenge motivates us to explore a more principled approach to represent 3D Gaussian Splatting in neural networks that preserves the underlying color and geometric structure while enforcing unique mapping and channel homogeneity. In this paper, we propose an embedding representation of 3DGS based on continuous submanifold fields that encapsulate the intrinsic information of Gaussian primitives, thereby benefiting the learning of 3DGS.

1 INTRODUCTION

Recent advances in 3D Gaussian Splatting (3DGS) (Kerbl et al., 2023) have established it as a powerful technique for representing and rendering 3D scenes, enabling high-fidelity, real-time novel view synthesis through explicit parameterization of Gaussian primitives. This representation has catalyzed a growing body of work exploring learning-based methods that operate directly on Gaussian primitives, supporting tasks such as compression (Shin et al., 2025), generation (Yi et al., 2024; Xie et al., 2025), and understanding (Guo et al., 2024). In these pipelines, the native parameterization $\theta = \{\mu, \mathbf{q}, \mathbf{s}, \mathbf{c}, o\}$ is often adopted as the input or output of neural architectures.

Despite its effectiveness in optimization-based reconstruction, we identify fundamental limitations when this parametric representation is employed as a learning space for neural networks. Our analysis reveals three critical issues. First, the mapping from parameters to rendered output exhibits non-uniqueness: multiple distinct parameter configurations yield identical visual results. This occurs through quaternion sign ambiguity (i.e., \mathbf{q} and $-\mathbf{q}$ represent identical rotations), symmetry-induced rotation invariance, and equivalences in spherical harmonic coefficients. Second, the parameter components exhibit severe numerical heterogeneity, with scales spanning large magnitude while quaternions remain unit-normalized. Third, these parameters inherently reside on distinct mathematical manifolds: positions in \mathbb{R}^3 , rotations in $SO(3)$, and appearance in spherical harmonic space, inconsistent with the Euclidean space demands of standard neural architectures.

These theoretical limitations translate into substantial practical failures. Our empirical analysis reveals critical instabilities: negating quaternion values, which should produce equivalent rotations, causes complete decoding failure in parameter-trained autoencoders (see App. Fig. 8). Parametric representations achieve lower reconstruction quality and exhibit severe degradation under domain shift, particularly when transferring from object-level to scene-level data. Moreover, parametric embeddings lack robustness to noise, with minor perturbations causing disproportionate reconstruction errors. These consistent failures indicate fundamental representation deficiencies.

We thus propose a principled alternative: representing each Gaussian primitive as a continuous field defined on its iso-probability surface. This submanifold field representation establishes a unique relationship between Gaussians and their geometric-photometric properties, eliminating the ambiguity

[†] Corresponding author.

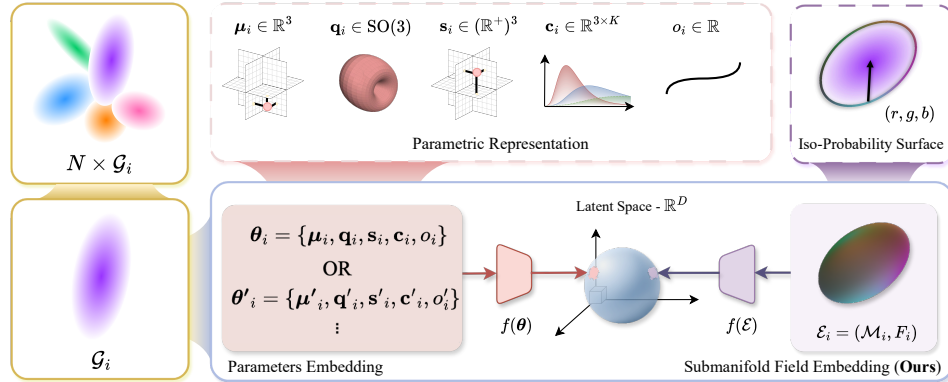


Figure 1: A scene of N Gaussian primitives can be represented by N sets of parameters θ (shown in pink). Data in this parametric space resides on different manifolds and is heterogeneous and non-Euclidean, introducing challenges for encoders to fit disparate data manifolds implicitly. Shown in purple is the proposed representation, instead of relying on Gaussian parameterization, we introduce a canonical submanifold field space (\mathcal{M}, F) that uniquely represents a Gaussian primitive with an iso-probability surface.

inherent in parametric representations. By discretizing this field as a colored point cloud sampled from the probability surface, we obtain a representation that maintains uniform numerical properties and respects the underlying geometric structure. Particularly, we employ a variational autoencoder to learn embeddings from discretized submanifold fields, introducing a Manifold Distance metric based on optimal transport that better aligns with perceptual quality than parameter-space distances. Extensive experiments demonstrate substantial improvements in reconstruction quality, superior cross-domain generalization, and more robust latent representations compared to parametric baselines. The learned embeddings exhibit better noise resilience and semantic structure, validating our submanifold field representation as a more suitable learning space for 3D Gaussian primitives.

To summarize the contribution of this work, we:

- identify and formally characterize the fundamental limitations of parametric Gaussian representations for neural learning, including non-uniqueness and numerical heterogeneity.
- propose a submanifold field representation that provides provably unique and geometrically consistent encoding of Gaussian primitives.
- develop a variational autoencoder framework incorporating a novel Manifold Distance metric based on optimal transport theory for effective learning in the submanifold field representation space with extensive experimental evidence.

2 RELATED WORKS

3D Gaussian Splatting. Since its re-introduction by Kerbl et al. (2023), 3DGS has rapidly become a core method for novel view synthesis and 3D representation. By placing explicit Gaussian primitives in 3D space and employing efficient rasterization and accumulation, 3DGS achieves real-time rendering with high fidelity (Bao et al., 2025; Lin et al., 2025c). Several studies improve efficiency (Jo et al., 2024; Lee et al., 2024), while others leverage large-scale datasets for generalization (Ma et al., 2025; Li et al., 2025a). At the application level, 3DGS has been adopted for digital human (Li et al., 2024; Kocabas et al., 2024; Wang et al., 2025), self-driving scene modeling (Zhou et al., 2024a;c; Yan et al., 2023), and physics-based simulation (Jiang et al., 2024; Xie et al., 2024; Zhong et al., 2024). Beyond fixed Gaussian parameters, another line augments primitives with latent embeddings to capture semantics, open-vocabulary understanding (Qin et al., 2024) and deformation modeling (Zhobro et al., 2025). These efforts demonstrate that 3DGS provides high-fidelity appearance and serves as a versatile representation with broad potential (Sun et al., 2025).

3DGS Parameters Regression. To enable fast and flexible reconstruction without per-scene optimization, recent works seek to directly obtain Gaussian splats through feedforward prediction networks. For example, Charatan et al. (2024); Chen et al. (2024b) proposed to predict Gaussian

parameters directly from multi-view input, while Zheng et al. (2024) generate pixel-wise parameter maps and lift them to 3D via depth estimation. This paradigm has been extended to pose-free settings (Hong et al., 2024; Chen et al., 2024c; Tian et al., 2025), and transformer-based methods further improve scalability and generalization (Li et al., 2025b; Jiang et al., 2025; Lin et al., 2025b). Overall, these methods directly output Gaussian parameters from neural networks, showing that 3DGS can serve as an effective target for network-based prediction in efficient reconstruction.

Embedding Gaussian Primitives. Recent works move beyond reconstruction and encode Gaussian parameters into latent spaces for tasks such as generation, editing, and compression. Zhou et al. (2024b); Lin et al. (2025a); Wewer et al. (2024) learn structured latent variables from 3D Gaussian space to fulfill generation tasks. Editing and style-transfer methods use diffusion or style conditioning to manipulate Gaussians primitives in latent or rendering spaces (Chen et al., 2024a; Vachha & Haque, 2024; Lee et al., 2025; Palandra et al., 2024; Zhang et al., 2024; Kovács et al., 2024; Yu et al., 2024). Other works improve rendering quality by optimizing Gaussian parameters under diffusion priors (Tang et al., 2023; Yi et al., 2024; Chen et al., 2024d), while compression methods (Girish et al., 2024; Yang et al., 2025) reduce storage and computation by quantizing and embedding Gaussian parameters. These approaches show the potential of embedding Gaussians into neural latent spaces, but they assume Gaussian parameters are naturally compatible with neural learning, overlooking that these parameters were designed for optimization-based reconstruction. This oversight underlies our analysis in Section 3 and our proposal of a more suitable formulation.

3 METHOD

3.1 PRELIMINARIES: GAUSSIAN SPLATTING PARAMETERIZATION

A scene under 3D Gaussian Splatting is represented as a set of N oriented, and view-dependently colored Gaussian primitives $\{\mathcal{G}_i\}_{i=1}^N$, each contributing to the final rendered image via rasterization and alpha compositing. Each Gaussian primitive \mathcal{G}_i is usually represented by a parameter tuple $\theta_i = \{\mu_i, \mathbf{q}_i, \mathbf{s}_i, \mathbf{c}_i, o_i\}$, where:

- $\mu_i \in \mathbb{R}^3$: the center position of the Gaussian in world coordinates;
- $\mathbf{q}_i \in \text{SO}(3)$: a unit quaternion representing the local rotation;
- $\mathbf{s}_i \in (\mathbb{R}^+)^3$: scale parameters along the rotated axes;
- $\mathbf{c}_i \in \mathbb{R}^{3 \times K}$: spherical harmonic (SH) coefficients for view-dependent color for $K \in \mathbb{Z}$;
- $o_i \in \mathbb{R}$: a logit-transformed opacity value $\alpha_i = \sigma(o_i)$, where σ is a sigmoid function.

The local geometry of the Gaussian is governed by its covariance matrix, constructed as

$$\Sigma_i = R(\mathbf{q}_i) \text{diag}(\mathbf{s}_i)^2 R(\mathbf{q}_i)^\top, \quad (1)$$

where $R(\mathbf{q}_i)$ is the rotation matrix corresponding to the quaternion \mathbf{q}_i . This defines an ellipsoidal spatial density, centered at μ_i , whose shape and orientation determine the contribution of \mathcal{G}_i to the rendered scene. The color at a given view direction $\mathbf{d} \in \mathbb{S}^2$ is computed per channel using SH basis functions denoted by

$$\text{Color}_i(\mathbf{d}) = \left[\text{SH}_i^c(\mathbf{d}), \text{SH}_i^g(\mathbf{d}), \text{SH}_i^b(\mathbf{d}) \right]^\top, \quad (2)$$

where $\text{SH}_i^c(\mathbf{d})$ in c -channel is calculated by $\sum_{l=0}^{L_{\max}} \sum_{m=-l}^l (\mathbf{c}_i)_{c,(l,m)} \cdot Y_l^m(\mathbf{d})$. Y_l^m is the real-valued spherical harmonic of degree l and order m . The final rendering aggregates contributions from all \mathcal{G}_i via a soft visibility-weighted compositing process. This native parameterization is well-suited for gradient-based scene optimization. However, it introduces significant challenges when used as a representation for learning.

3.2 PARAMETERIZATION IS ILL-SUITED AS A LEARNING SPACE

The parameter representation θ poses fundamental challenges when used as a learning space for neural networks. We identify two critical issues: representation non-uniqueness and numerical heterogeneity. Each undermines the stability and effectiveness of neural network training.

Representation Non-uniqueness. The parametric representation suffers from a many-to-one mapping that violates basic requirements for stable learning. To understand this, we first formalize what rendering effect a single Gaussian primitive produces.

Definition 1 (Single Gaussian Radiance Field (SGRF)) A SGRF is a radiance field $\phi : \mathbb{R}^3 \times \mathbb{S}^2 \rightarrow \mathbb{R}^3$, the field is defined by the local density at point $\mathbf{x} \in \mathbb{R}^3$ along direction $\mathbf{d} \in \mathbb{S}^2$:

$$\phi_{\mathcal{G}}(\mathbf{x}, \mathbf{d}) = \rho_{\mathcal{G}}(\mathbf{x}) \cdot c_{\mathcal{G}}(\mathbf{d}), \quad (3)$$

where $\rho_{\mathcal{G}}(\mathbf{x}) = \exp(-\frac{1}{2}(\mathbf{x} - \boldsymbol{\mu})^\top \Sigma^{-1}(\mathbf{x} - \boldsymbol{\mu}))$ is a volume density function and $c_{\mathcal{G}}(\mathbf{d})$ is a color radiance field coupled with opacity. Specifically, given a parameter set $\boldsymbol{\theta} = \{\boldsymbol{\mu}, \mathbf{q}, \mathbf{s}, \mathbf{c}, o\}$, Σ can be derived by equation 1 and $c_{\mathcal{G}}(\mathbf{d}) = \sigma(o) \cdot \text{Color}(\mathbf{d})$ can be derived by equation 2.

The SGRF, derived from the multi-Gaussian rendering framework by Kerbl et al. (2023), specifies how the final value at any pixel is rendered in a scene containing only one Gaussian splat. Furthermore, let Φ be the space of SGRFs, and $\Theta \subseteq \mathbb{R}^{|\boldsymbol{\theta}|}$ be the parameter space of Gaussian primitives, each parameter set $\boldsymbol{\theta} \in \Theta$ provides a complete representation that generates a corresponding field $\phi_{\mathcal{G}} \in \Phi$. We indicate that a single SGRF may correspond to multiple parameterizations of Gaussian primitives, as formalized in the following proposition.

Proposition 1 (Non-uniqueness of the SGRF Parametric Representation) The parametric representation of a SGRF is not unique. Formally, there exist at least two distinct parameter sets, $\boldsymbol{\theta}_1 \in \Theta$ and $\boldsymbol{\theta}_2 \in \Theta$ with $\boldsymbol{\theta}_1 \neq \boldsymbol{\theta}_2$, that generate the exact same field $\phi_{\mathcal{G}} \in \Phi$.

The non-uniqueness is from quaternion sign ambiguity, geometric symmetries, and rotation-spherical harmonic interactions producing equivalent parameter combinations (see Appendix for proof). The non-uniqueness of $\boldsymbol{\theta}$ will create “embedding collisions” where different parameter vectors produce identical rendered output (Wang & Isola, 2020). This makes the learning objective $\|\boldsymbol{\theta}_{\text{pred}} - \boldsymbol{\theta}_{\text{target}}\|_p$ ambiguous, as multiple parameter configurations can achieve the same visual result. The resulting conflicting gradients lead to training instability and poor convergence indicated by Bengio et al. (2013).

Numerical Heterogeneity The parameter components violate the homogeneous distribution assumption of standard neural architectures. Neural networks typically assume features share similar statistical properties for effective gradient flow (Ioffe & Szegedy, 2015). However, 3D Gaussian parameters span vastly different ranges. For example, pre-activation scales can range from -15 to 3 , while quaternions stay unit-normalized. More fundamentally, these parameters follow different distributions and live on different manifolds: positions $\boldsymbol{\mu} \in \mathbb{R}^3$, rotations $\mathbf{q} \in \text{SO}(3)$, scales $\mathbf{s} \in (\mathbb{R}^+)^3$, and SH coefficients \mathbf{c} with exponential decay. Concatenating them ignores their heterogeneous nature. Small noises in quaternions can drastically alter geometry, while small noise in high-order SH coefficients is negligible, yet the network treats all dimensions equally.

The non-uniqueness and numerical heterogeneity of the native parameter space $\boldsymbol{\theta}$ make it unsuitable for neural network learning, which would generate unstable embeddings (see our experiments in Sec. 4.4 and App. D). We therefore introduce a submanifold field representation that ensures unique mappings and respects the geometric structure of 3D Gaussians.

3.3 REPRESENTATION ON SUBMANIFOLD FIELD

To address this issue, we propose converting each Gaussian primitive \mathcal{G}_i to a novel geometric representation \mathcal{E}_i , which is a color field defined on a 2D submanifold in 3D Euclidean space, as illustrated in Fig. 1. For a Gaussian density $\mathcal{N}(\mathbf{x}; \boldsymbol{\mu}_i, \Sigma_i)$, we define the iso-probability surface at fixed radius r as:

$$\mathcal{M}_i = \{\mathbf{x} \in \mathbb{R}^3 \mid (\mathbf{x} - \boldsymbol{\mu}_i)^\top \Sigma_i^{-1}(\mathbf{x} - \boldsymbol{\mu}_i) = r^2\}, \quad (4)$$

which forms an ellipsoid surface, namely, a two-dimensional submanifold, centered at $\boldsymbol{\mu}_i$. On this submanifold, we define a field function:

$$F_i(\mathbf{x}) = \sigma(o_i) \cdot \text{Color}_i(\mathbf{d}_{\mathbf{x}}), \quad (5)$$

where $\mathbf{d}_{\mathbf{x}} = (\mathbf{x} - \boldsymbol{\mu}_i) / \|\mathbf{x} - \boldsymbol{\mu}_i\|$ denotes the unit direction vector for $\mathbf{x} \in \mathcal{M}_i$, and $\text{Color}_i(\cdot)$ represents the view-dependent color parameterization as in equation 2. Let \mathbb{M} be the space of all

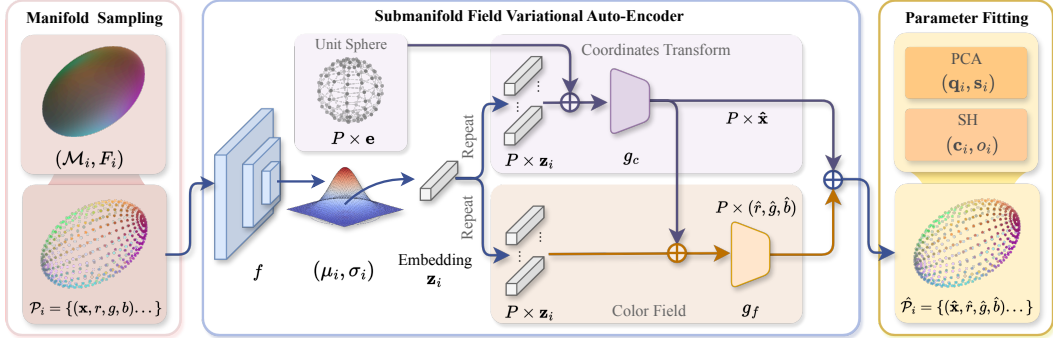


Figure 2: To embed the proposed submanifold field representation into a vector form suitable for neural networks, we devise a submanifold field variational auto-encoder (SF-VAE) that embeds any input submanifold field as a 32-D vector, then reconstructs the original parameter set θ_i . SF-VAE learns in our new representation space instead of the parametric space.

possible iso-probability submanifolds as defined in equation 4, we define our unified representation space as:

$$\mathcal{E} = \{\mathcal{E}_i = (\mathcal{M}_i, F_i) \mid \mathcal{M}_i \in \mathbb{M}, F_i : \mathcal{M}_i \rightarrow \mathbb{R}^3\}, \quad (6)$$

The representation $\mathcal{E}_i \in \mathcal{E}$ encodes both geometric properties (shape, orientation) via \mathcal{M}_i and appearance attributes (view-dependent color) via F_i in a continuous framework. We have the following proposition (proof is provided in App. B).

Proposition 2 (Uniqueness of Submanifold Field Representation) *For every SGRF $\phi_{\mathcal{G}} \in \Phi$, there exists a unique corresponding representation $\mathcal{E} \in \mathcal{E}$. This establishes a one-to-one correspondence between the elements of Φ and \mathcal{E} . Formally, for any two distinct fields $\phi_{\mathcal{G},1}, \phi_{\mathcal{G},2} \in \Phi$, their corresponding representations $\mathcal{E}_1, \mathcal{E}_2 \in \mathcal{E}$ are also distinct.*

The submanifold field \mathcal{E}_i thus provides a numerically stable and provably unique representation space on which we can safely build learning objectives and neural architectures.

3.4 ENCODE SUBMANIFOLD FIELDS AS EMBEDDINGS

We design a variational auto-encoder to encode submanifold field representation, shown in Fig. 2. The network architecture, learning objectives and dataset are introduced.

Encoder-decoder Architecture. We employ a point-cloud-based network to encode and decode one sub-manifold field. Particularly, we uniformly sample P points from the submanifold field \mathcal{E} as a colored point cloud $\mathcal{P} = \{(\mathbf{x}_m, F(\mathbf{d}_{\mathbf{x}_m}))\}_{m=1}^P$. We then employ a PointNet (Qi et al., 2017) encoder f to obtain latent embedding by $\mathbf{z} \sim f(\mathbf{z} \mid \mathcal{P})$ where $\mathbf{z} \in \mathbb{R}^D$ is the embedding with dimension D . The decoder g consists of two neural networks, namely, the coordinates transform network $g_c : \mathbb{R}^3 \times \mathbb{R}^D \rightarrow \mathbb{R}^3$ and color field $g_f : \mathbb{R}^3 \times \mathbb{R}^D \rightarrow \mathbb{R}^3$. The decoded point cloud from decoder is given by,

$$\hat{\mathcal{P}} = g(\mathbf{z}, \mathcal{U}_{P'}) = \{g_c([\mathbf{e}_n, \mathbf{z}]), g_f([g_c([\mathbf{e}_n, \mathbf{z}]), \mathbf{z}])\}_{n=1}^{P'} \quad (7)$$

where $\mathcal{U}_{P'} = \{\mathbf{e}_n\}_{n=1}^{P'}$ is a set of coordinates sampled from a unit sphere surface. Such canonical set works as the initial input for two implicit functions g_c and g_f , and queries new coordinates and color field. Furthermore, to recover the original Gaussian parameters θ_i for rendering purposes, we estimate the covariance matrix Σ_i by principal component analysis (PCA), and SH coefficients \mathbf{c}_i by fitting the spherical harmonics to $\hat{\mathcal{P}}$.

Learning Objectives. We introduce **Manifold Distance** (M-Dist) for the reconstruction objective in encoder-decoder training. Given two submanifold fields $\mathcal{E} = (\mathcal{M}, F)$ and $\hat{\mathcal{E}} = (\hat{\mathcal{M}}, \hat{F})$, we propose to measure their similarity based on the Wasserstein-2 distance from optimal transport defined as

$$W_2^2(\mathcal{E}, \hat{\mathcal{E}}) = \inf_{\gamma \in \Gamma(\hat{\mathcal{P}}, \hat{\mathcal{P}}')} \int_{\mathcal{M} \times \hat{\mathcal{M}}} d^2((\mathbf{x}, c_x), (\mathbf{y}, c_y)) d\gamma(\mathbf{x}, \mathbf{y}) \quad (8)$$

where $c_x = F(\mathbf{d}_x)$, $c_y = \hat{F}(\mathbf{d}_y)$, $\Gamma(\hat{\sigma}_i, \hat{\sigma}_j)$ is the set of all joint probability measures (transport plans) with marginals $\hat{\sigma}_i$ and $\hat{\sigma}_j$, and the ground distance is defined as

$$d^2((\mathbf{x}, c_x), (\mathbf{y}, c_y)) = \|\mathbf{x} - \mathbf{y}\|_2^2 + \lambda \|c_x - c_y\|_2^2, \quad (9)$$

with $\lambda \in \mathbb{R}^+$ balancing spatial and color terms. In practice, both \mathcal{M} and $\hat{\mathcal{M}}$ are discretized as colored point clouds \mathcal{P} and $\hat{\mathcal{P}}$. The empirical Wasserstein-2 distance \hat{W} is then computed between these point clouds by

$$\hat{W}_2^2(\mathcal{P}, \hat{\mathcal{P}}) = \min_{\Gamma \in \Gamma(\hat{\sigma}, \hat{\sigma}')} \sum_{(\mathbf{x}_i, c_{x_i}) \in \mathcal{P}} \sum_{(\mathbf{y}_j, c_{y_j}) \in \hat{\mathcal{P}}} \Gamma_{ij} (d^2((\mathbf{x}_i, c_{x_i}), (\mathbf{y}_j, c_{y_j}))). \quad (10)$$

Finally, the learning objective for variational auto-encoder is

$$\mathcal{L}_{\text{VAE}} = \mathbb{E}_{\hat{\mathcal{P}} \sim \text{VAE}(\mathcal{P})} \left(\hat{W}_2^2(\mathcal{P}, \hat{\mathcal{P}}) + \beta \cdot d_{\text{KL}}(f(\mathbf{z} \mid \mathcal{P}) \parallel \mathcal{N}(0, \mathbf{I})) \right), \quad (11)$$

where $\text{VAE}(\mathcal{P}) = g(f(\mathbf{z} \mid \mathcal{P}), \mathcal{U}_{P'})$ and the second term is the KL divergence loss for variational auto-encoder implementation, and β is a balance factor.

Dataset Preparation. Since this embedding model only encodes single Gaussian primitives, which have no semantic meaning out of a scene’s global context, we can use a *randomly generated dataset* of Gaussian primitives to train this model, thus making it domain-invariant to data. The implementation details of this generated dataset can be found in App. C.

4 EXPERIMENTS

4.1 EVALUATION SETUP

Baseline Implementation Details. To isolate the effect of representation choice, we adopt a self-implemented encoder–decoder framework for both the parametric representation θ and the proposed submanifold field representation \mathcal{E} . While comparisons with existing 3DGS learning methods are possible, they typically involve task-specific architectures that confound the role of representation itself. Direct reuse of prior pipelines would not yield a controlled comparison, so we implement both baselines in the same VAE-style framework to attribute differences solely to the representation.

We implement and train three size-matched embedding models: our submanifold field VAE (Sec. 3.4), and two baseline parametric VAEs operating directly on θ . For the parametric models, each Gaussian primitive is represented as a 56-D vector (3+4+3K+1 for $L_{\text{max}}=3$), omitting global coordinates to match the SF-VAE setting. A three-layer MLP encodes this input to a 32-D latent (56 \rightarrow 512 \rightarrow 512 \rightarrow 32 \times 2), and the decoder, either uses a MLP to map the latent back to $\hat{\theta}_i$, or uses the same decoder of SF-VAE to map to $\hat{\mathcal{P}}$. This setting further decouples evaluation results with the training objective functions. Apart from input dimension, all models share identical depth, width, latent size (32), and optimizer settings, ensuring a matched capacity.

Datasets. We evaluate the proposed representation and compare it with the baseline primarily using two datasets. For object-level tasks, we utilize ShapeSplat (Ma et al., 2025), a large-scale 3DGS dataset derived from ShapeNet (Chang et al., 2015), comprising 52K objects across 55 categories. For scene-level experiments, we employ Mip-NeRF 360 (Barron et al., 2022), which contains 7 medium-scale scenes with abundant high-frequency details. Additionally, unless stated otherwise, we train the embedding models using the randomly generated Gaussian primitive dataset, with 500K randomly generated data samples; implementation details are provided in App. C.

Evaluation Metrics. To comprehensively assess both perceptual fidelity and representation quality, we report PSNR, SSIM, and LPIPS on rasterized reconstructions against ground truth Gaussian splats, as well as L_1 distance in the Gaussian parameter space. Crucially, we also include our proposed Manifold Distance (M-Dist) as an evaluation criterion. By cross-comparing M-Dist with parameter-space distances (L_1/L_2), we can demonstrate that M-Dist aligns more closely with perceptual “gold standard” metrics such as PSNR and LPIPS, validating our claims in Sec. 3

Table 1: Reconstruction quality comparison for object-level (ShapeSplat) and scene-level (Mip-NeRF 360) datasets. All models trained on the randomly generated dataset. The three models have a parameter count of 0.62M, 0.66M and 0.62M respectively. The relatively extreme perceptual metrics values in ShapeSplat come from the use of background during measurement.

Input Representation	Encoder	Decoder	PSNR \uparrow	SSIM \uparrow	LPIPS \downarrow	M-Dist	L_1 -Dist
ShapeSplat							
Parametric	MLP	MLP	37.512	0.888	0.152	0.184	<u>0.040</u>
Parametric	MLP	SF-VAE	44.725	0.896	0.136	0.051	0.097
Submanifold Field	SF-VAE	SF-VAE	63.408	0.990	0.010	<u>0.041</u>	0.098
Mip-NeRF 360							
Parametric	MLP	MLP	18.818	0.564	0.452	0.510	0.034
Parametric	MLP	SF-VAE	20.923	0.730	0.359	0.055	0.173
Submanifold Field	SF-VAE	SF-VAE	29.833	0.953	0.079	<u>0.048</u>	0.179



Figure 3: Qualitative results for rasterized reconstruction. Samples selected arbitrarily from Mip-NeRF 360 and ShapeSplat. Parametric models can induce confusion in rotation space, failing to predict the correct rotation.

4.2 QUANTITATIVE RECONSTRUCTION RESULTS

We present a comprehensive quantitative and qualitative analysis of reconstruction quality for both object-level and scene-level data, as summarized in Tab. 1 and Fig. 3. All models are trained on the same randomly generated 3D Gaussian primitives dataset and evaluated on ShapeSplat and Mip-NeRF 360, using three matched encoder-decoder configurations to control for bias. Across all perceptual metrics (PSNR, SSIM, LPIPS), the submanifold field representation consistently outperforms parametric baselines. For example, on ShapeSplat, SF-VAE achieves substantially higher PSNR and SSIM and a much lower LPIPS, indicating both improved fidelity and perceptual quality. Similar performance gains are observed in scene-level reconstruction, where the submanifold field model demonstrates better performance across diverse spatial contexts.

Importantly, the Manifold Distance (M-Dist) metric shows a stronger empirical correlation with perceptual metrics like PSNR and LPIPS than traditional L_1 parameter distances, supporting our claim that M-Dist is a more robust and meaningful similarity measure for 3D Gaussian representations, truthfully reflecting perceptual differences rather than merely parameter discrepancies. The consistent improvement margin across both datasets highlights the advantage of learning in the submanifold field space, which better preserves intrinsic structure and view-dependent appearance, confirming the efficacy of our representation for high-fidelity 3D Gaussian modeling.

Table 2: Results on representation generalization: train on one dataset, test on the other.

Train set	Test set	Input Represent.	Encoder / Decoder	PSNR \uparrow	SSIM \uparrow	LPIPS \downarrow
ShapeSplat	Mip-NeRF.	Parametric	MLP / MLP	9.753	0.356	0.615
		Parametric	MLP / SF-VAE	14.845	0.675	0.336
		Submanifold Field	SF-VAE / SF-VAE	19.194	0.821	0.309
Mip-NeRF.	ShapeSplat	Parametric	MLP / MLP	55.624	0.957	0.067
		Parametric	MLP / SF-VAE	60.777	0.987	0.013
		Submanifold Field	SF-VAE / SF-VAE	62.576	0.990	0.014



Figure 4: Parametric results use MLP encoder and SF-VAE’s decoder. Left: Sample visual comparison on robustness to noise in embedding space. Right: Comparison on M-Dist for different noise levels added to embedding space, tested on Mip-NeRF 360.

4.3 CROSS-DOMAIN GENERALIZATION

We evaluate cross-domain generalization by training on one dataset and testing on the other (object-level \leftrightarrow scene-level) under an identical training protocol and capacity budget as in the reconstruction study. Concretely, we train either the proposed SF-VAE or the parametric MLP baselines on a source set and evaluate zero-shot on a target set, rendering novel views and reporting PSNR, SSIM, and LPIPS averaged over test samples (see Tab. 2).

Across both transfer directions, the submanifold field model consistently achieves higher reconstruction quality than the parametric baseline, with the largest margins when transferring from object-level sources to larger-scale scenes, indicating reduced sensitivity to dataset-specific statistics (scale, lighting, SH complexity).

4.4 LATENT SPACE EVALUATION

Robustness to Noise. To evaluate the submanifold field embedding’s robustness to noise, we gradually add higher levels of gaussian noise to the embedding space of each representation and test their reconstruction quality and M-Dist. As shown in Fig. 4, the embedding space of submanifold field model is more robust to random perturbation, this makes submanifold field embeddings a better learning target since it is less sensitive to potential systematic noise.

Latent Space Clustering. To further probe the semantic structure of the learned embedding spaces, we perform unsupervised graph clustering on both the raw Gaussian parameter space and the embedding outputs of each model. As visualized in Fig. 5, clusters formed in the submanifold field embedding space exhibit more detailed semantic separation against the reference images compared to those formed using normalized parameters or parametric embeddings. For example, SF-VAE’s embedding clustering in the first line of Fig. 5 outlines clearer separation of foreground objects with the background. The clusters appear smoother, less noisy, and with clearer boundaries, showing an ability to distinguish between different entities. This indicates that the submanifold field embedding captures more dense semantics and discriminative features, validating its usefulness.

Latent Space Interpolation. To evaluate the regularity of the latent space of the proposed representation, we randomly sample pairs of source and target Gaussian primitives \mathcal{G}_s and \mathcal{G}_t and linearly interpolate each pair for a fixed number of steps $n = 7$. Compared with parametric space, the interpolation in submanifold field embedding space shows a smooth transition path, while interpolation in parametric space shows undesired jitter in rotation and scale, indicating space irregularities, see App. D. This highlights the motivation to learn in the unified submanifold field embedding space.

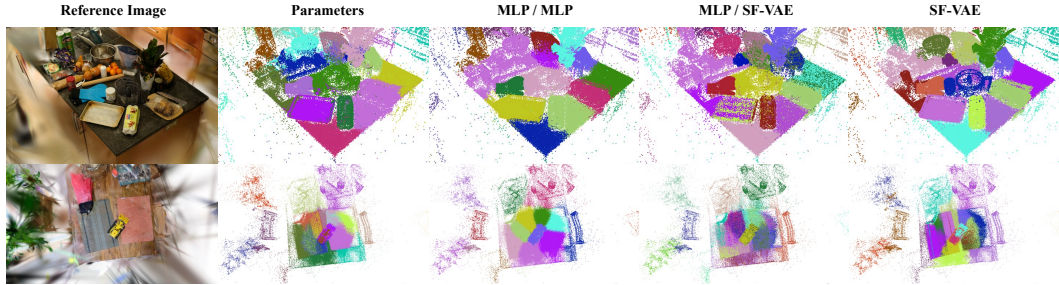


Figure 5: Qualitative evaluation of unsupervised graph clustering, compared using Gaussian parameters and the embedding of the respective models, using the same hyperparameters. Submanifold field embeddings show better preservation of detailed semantics, validating its usefulness.

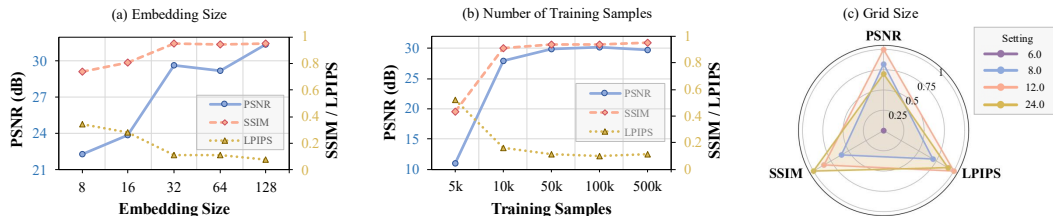


Figure 6: Ablation study results, tested on Mip-NeRF 360. From left to right: (a) embedding space dimension, (b) generated training dataset size, (c) Submanifold Field sample size (all values normalized to $[0, 1]$, with LPIPS inversely normalized).

4.5 MORE STUDIES

Latent Space Dimension. We evaluated different embedding space dimensions for the SF-VAE model to meet the best trade-off between compression and reconstruction quality. All models are trained on the generated dataset with $L = 3$ order Spherical Harmonics. Results shown in Fig. 6 (a), 32 is the optimal balance point between reconstruction quality and latent space compression. All values are tested with baseline input/output of $P = 12^2$. While this work does not specifically focus on compression effectiveness, embedding space robustness shown in Sec. 4.4 suggests potential in further latent tokenization and quantization.

Size of Training Set. To empirically determine the number of random training samples required to achieve the best reconstruction results, we tested a wide spectrum of training sample sizes, ranging from 5K to 500K (baseline). The results indicate the proposed representation is data efficient. When only using 2% of the baseline training sample, our model can achieve close-to-baseline performance.

Point Sample Size of Submanifold Fields. To ensure the submanifold fields are truthfully represented in a discrete manner, we evaluate different sample sizes P . Going from the lowest tested $P = 6^2$ to the baseline $P = 12^2$, we observe a gradual improvement in reconstruction quality, while going above $P = 12^2$ yields very little improvement. Since P directly correlates to the computational efficiency of the submanifold field model (see below), we keep $P = 12^2$.

Computational Efficiency. Increasing the point sample size P leads to higher compute time and memory consumption. Encoding time stays low since a lightweight PointNet-based encoder shares weights with all input points, ensuring efficient encoding of large-scale scenes, with an inference speed of 1.72s per 1 million Gaussians for $P = 12^2$ using a batch size of 4096 on an RTX 5090. Query time during decoding is $O(P)$ which is $O(n^2)$ w.r.t. the grid size n . When the computation is not bottlenecked and uses a large enough batch size, the amortized time complexity is $\Theta(n)$.

5 CONCLUSION AND LIMITATIONS

We introduced a geometry-aware *submanifold field* representation for 3D Gaussian Splatting that maps each primitive to a color field on a canonical iso-probability ellipsoid and proved the mapping is injective over core attributes. Built on this representation, our SF-VAE learns semantically meaningful latents and yields higher-fidelity reconstructions and stronger zero-shot generalization than

capacity-matched raw-parameter baselines; our manifold distance (M-Dist) further aligns training and evaluation with geometric/perceptual similarity.

Limitations and Outlook. Our current setup operates at the single-Gaussian level, while this ensures data invariance, it omits explicit inter-splat structure modeling for more complex representation learning. Promising directions include set/scene-level encoders with permutation-invariant attention, point cloud to 3DGS inpainting, generative modeling with submanifold field embeddings, temporal extensions to dynamic scenes, and applications to compression, retrieval, and regularization in broader 3DGS pipelines.

REFERENCES

Yanqi Bao, Tianyu Ding, Jing Huo, Yaoli Liu, Yuxin Li, Wenbin Li, Yang Gao, and Jiebo Luo. 3d gaussian splatting: Survey, technologies, challenges, and opportunities. *IEEE Transactions on Circuits and Systems for Video Technology*, 2025.

Jonathan T Barron, Ben Mildenhall, Dor Verbin, Pratul P Srinivasan, and Peter Hedman. Mip-nerf 360: Unbounded anti-aliased neural radiance fields. In *CVPR*, 2022.

Yoshua Bengio, Aaron Courville, and Pascal Vincent. Representation learning: A review and new perspectives. *IEEE transactions on pattern analysis and machine intelligence*, 35(8):1798–1828, 2013.

Angel X Chang, Thomas Funkhouser, Leonidas Guibas, Pat Hanrahan, Qixing Huang, Zimo Li, Silvio Savarese, Manolis Savva, Shuran Song, Hao Su, et al. Shapenet: An information-rich 3d model repository. *arXiv preprint arXiv:1512.03012*, 2015.

David Charatan, Sizhe Lester Li, Andrea Tagliasacchi, and Vincent Sitzmann. pixelsplat: 3d gaussian splats from image pairs for scalable generalizable 3d reconstruction. In *CVPR*, 2024.

Yiwen Chen, Zilong Chen, Chi Zhang, Feng Wang, Xiaofeng Yang, Yikai Wang, Zhongang Cai, Lei Yang, Huaping Liu, and Guosheng Lin. Gaussianeditor: Swift and controllable 3d editing with gaussian splatting. In *CVPR*, 2024a.

Yuedong Chen, Haofei Xu, Chuanxia Zheng, Bohan Zhuang, Marc Pollefeys, Andreas Geiger, Tat-Jen Cham, and Jianfei Cai. Mvsplat: Efficient 3d gaussian splatting from sparse multi-view images. In *ECCV*, 2024b.

Zequn Chen, Jiezhi Yang, and Heng Yang. Pref3r: Pose-free feed-forward 3d gaussian splatting from variable-length image sequence. *arXiv preprint arXiv:2411.16877*, 2024c.

Zilong Chen, Feng Wang, Yikai Wang, and Huaping Liu. Text-to-3d using gaussian splatting. In *CVPR*, 2024d.

Sharath Girish, Kamal Gupta, and Abhinav Shrivastava. Eagles: Efficient accelerated 3d gaussians with lightweight encodings. In *ECCV*, 2024.

Jun Guo, Xiaojian Ma, Yue Fan, Huaping Liu, and Qing Li. Semantic gaussians: Open-vocabulary scene understanding with 3d gaussian splatting. *arXiv preprint arXiv:2403.15624*, 2024.

Sunghwan Hong, Jaewoo Jung, Heeseong Shin, Jisang Han, Jiaolong Yang, Chong Luo, and Seunghyong Kim. Pf3plat: Pose-free feed-forward 3d gaussian splatting. *ICML*, 2024.

Sergey Ioffe and Christian Szegedy. Batch normalization: Accelerating deep network training by reducing internal covariate shift. In *ICML*, 2015.

Lihan Jiang, Yucheng Mao, Lining Xu, Tao Lu, Kerui Ren, Yichen Jin, Xudong Xu, Mulin Yu, Jiangmiao Pang, Feng Zhao, et al. Anysplat: Feed-forward 3d gaussian splatting from unconstrained views. *arXiv preprint arXiv:2505.23716*, 2025.

Ying Jiang, Chang Yu, Tianyi Xie, Xuan Li, Yutao Feng, Huamin Wang, Minchen Li, Henry Lau, Feng Gao, Yin Yang, et al. Vr-gs: A physical dynamics-aware interactive gaussian splatting system in virtual reality. In *SIGGRAPH*, 2024.

Joongho Jo, Hyeongwon Kim, and Jongsun Park. Identifying unnecessary 3d gaussians using clustering for fast rendering of 3d gaussian splatting. *arXiv preprint arXiv:2402.13827*, 2024.

Bernhard Kerbl, Georgios Kopanas, Thomas Leimkühler, and George Drettakis. 3d gaussian splatting for real-time radiance field rendering. *ACM Trans. Graph.*, 2023.

Muhammed Kocabas, Jen-Hao Rick Chang, James Gabriel, Oncel Tuzel, and Anurag Ranjan. Hugs: Human gaussian splats. In *CVPR*, 2024.

Áron Samuel Kovács, Pedro Hermosilla, and Renata G Raidou. G-style: Stylized gaussian splatting. In *Computer Graphics Forum*, 2024.

Dong In Lee, Hyeongcheol Park, Jiyoung Seo, Eunbyung Park, Hyunje Park, Ha Dam Baek, Sangheon Shin, Sangmin Kim, and Sangpil Kim. Editsplat: Multi-view fusion and attention-guided optimization for view-consistent 3d scene editing with 3d gaussian splatting. In *CVPR*, 2025.

Junseo Lee, Seokwon Lee, Jungi Lee, Junyong Park, and Jaewoong Sim. Gscore: Efficient radiance field rendering via architectural support for 3d gaussian splatting. In *Proceedings of the 29th ACM International Conference on Architectural Support for Programming Languages and Operating Systems, Volume 3*, pp. 497–511, 2024.

Yue Li, Qi Ma, Runyi Yang, Huapeng Li, Mengjiao Ma, Bin Ren, Nikola Popovic, Nicu Sebe, Ender Konukoglu, Theo Gevers, et al. Scenesplat: Gaussian splatting-based scene understanding with vision-language pretraining. *ICCV*, 2025a.

Zhe Li, Zerong Zheng, Lizhen Wang, and Yebin Liu. Animatable gaussians: Learning pose-dependent gaussian maps for high-fidelity human avatar modeling. In *CVPR*, 2024.

Zhiqi Li, Chengrui Dong, Yiming Chen, Zhangchi Huang, and Peidong Liu. Vicasplat: A single run is all you need for 3d gaussian splatting and camera estimation from unposed video frames. *arXiv preprint arXiv:2503.10286*, 2025b.

Chenguo Lin, Panwang Pan, Bangbang Yang, Zeming Li, and Yadong Mu. Diffsplat: Repurposing image diffusion models for scalable gaussian splat generation. *arXiv preprint arXiv:2501.16764*, 2025a.

Chin-Yang Lin, Cheng Sun, Fu-En Yang, Min-Hung Chen, Yen-Yu Lin, and Yu-Lun Liu. Longsplat: Robust unposed 3d gaussian splatting for casual long videos. *ICCV*, 2025b.

Xin Lin, Shi Luo, Xiaojun Shan, Xiaoyu Zhou, Chao Ren, Lu Qi, Ming-Hsuan Yang, and Nuno Vasconcelos. Hqgs: High-quality novel view synthesis with gaussian splatting in degraded scenes. In *The Thirteenth International Conference on Learning Representations*, 2025c.

Qi Ma, Yue Li, Bin Ren, Nicu Sebe, Ender Konukoglu, Theo Gevers, Luc Van Gool, and Danda Pani Paudel. A large-scale dataset of gaussian splats and their self-supervised pretraining. In *2025 International Conference on 3D Vision (3DV)*, 2025.

Francesco Palandra, Andrea Sancietti, Daniele Baieri, and Emanuele Rodola. Gsedit: Efficient text-guided editing of 3d objects via gaussian splatting. *arXiv preprint arXiv:2403.05154*, 2024.

Charles R Qi, Hao Su, Kaichun Mo, and Leonidas J Guibas. Pointnet: Deep learning on point sets for 3d classification and segmentation. In *Proceedings of the IEEE conference on computer vision and pattern recognition*, pp. 652–660, 2017.

Minghan Qin, Wanhua Li, Jiawei Zhou, Haoqian Wang, and Hanspeter Pfister. Langsplat: 3d language gaussian splatting. In *CVPR*, 2024.

Seungjoo Shin, Jaesik Park, and Sunghyun Cho. Locality-aware gaussian compression for fast and high-quality rendering. *arXiv preprint arXiv:2501.05757*, 2025.

Yipengjing Sun, Chenyang Wang, Shunyuan Zheng, Zonglin Li, Shengping Zhang, and Xiangyang Ji. Generalizable and relightable gaussian splatting for human novel view synthesis. *arXiv preprint arXiv:2505.21502*, 2025.

Jiaxiang Tang, Jiawei Ren, Hang Zhou, Ziwei Liu, and Gang Zeng. Dreamgaussian: Generative gaussian splatting for efficient 3d content creation. *arXiv preprint arXiv:2309.16653*, 2023.

Qijian Tian, Xin Tan, Yuan Xie, and Lizhuang Ma. Drivingforward: Feed-forward 3d gaussian splatting for driving scene reconstruction from flexible surround-view input. In *AAAI*, 2025.

Cyrus Vachha and Ayaan Haque. Instruct-gs2gs: Editing 3d gaussian splats with instructions, 2024. URL <https://instruct-gs2gs.github.io/>.

Tongzhou Wang and Phillip Isola. Understanding contrastive representation learning through alignment and uniformity on the hypersphere. In *International conference on machine learning*, pp. 9929–9939. PMLR, 2020.

Xiaoyuan Wang, Yizhou Zhao, Botao Ye, Xiaojun Shan, Weijie Lyu, Lu Qi, Kelvin CK Chan, Yinxiao Li, and Ming-Hsuan Yang. Holigs: Holistic gaussian splatting for embodied view synthesis. *NeurIPS*, 2025.

Christopher Wewer, Kevin Raj, Eddy Ilg, Bernt Schiele, and Jan Eric Lenssen. latentsplat: Autoencoding variational gaussians for fast generalizable 3d reconstruction. In *ECCV*, 2024.

Haozhe Xie, Zhaoxi Chen, Fangzhou Hong, and Ziwei Liu. Generative gaussian splatting for unbounded 3d city generation. In *Proceedings of the Computer Vision and Pattern Recognition Conference*, pp. 6111–6120, 2025.

Tianyi Xie, Zeshun Zong, Yuxing Qiu, Xuan Li, Yutao Feng, Yin Yang, and Chenfanfu Jiang. Physgaussian: Physics-integrated 3d gaussians for generative dynamics. In *CVPR*, 2024.

Yunzhi Yan, Haotong Lin, Chenxu Zhou, Weijie Wang, Haiyang Sun, Kun Zhan, Xianpeng Lang, Xiaowei Zhou, and Sida Peng. Street gaussians for modeling dynamic urban scenes.(2023). *arXiv preprint arXiv:2401.01339*, 2023.

Qi Yang, Le Yang, Geert Van Der Auwera, and Zhu Li. Hybrids: High-efficiency gaussian splatting data compression using dual-channel sparse representation and point cloud encoder. *arXiv preprint arXiv:2505.01938*, 2025.

Taoran Yi, Jiemin Fang, Junjie Wang, Guanjun Wu, Lingxi Xie, Xiaopeng Zhang, Wenyu Liu, Qi Tian, and Xinggang Wang. Gaussiaandreamer: Fast generation from text to 3d gaussians by bridging 2d and 3d diffusion models. In *CVPR*, 2024.

Xin-Yi Yu, Jun-Xin Yu, Li-Bo Zhou, Yan Wei, and Lin-Lin Ou. Instantstylegaussian: Efficient art style transfer with 3d gaussian splatting. *arXiv preprint arXiv:2408.04249*, 2024.

Dingxi Zhang, Yu-Jie Yuan, Zhuoxun Chen, Fang-Lue Zhang, Zhenliang He, Shiguang Shan, and Lin Gao. Stylizedgs: Controllable stylization for 3d gaussian splatting. *arXiv preprint arXiv:2404.05220*, 2024.

Shunyuan Zheng, Boyao Zhou, Ruizhi Shao, Boning Liu, Shengping Zhang, Liqiang Nie, and Yebin Liu. Gps-gaussian: Generalizable pixel-wise 3d gaussian splatting for real-time human novel view synthesis. In *CVPR*, 2024.

Mikel Zobro, Andreas René Geist, and Georg Martius. Learning 3d-gaussian simulators from rgb videos. *arXiv preprint arXiv:2503.24009*, 2025.

Licheng Zhong, Hong-Xing Yu, Jiajun Wu, and Yunzhu Li. Reconstruction and simulation of elastic objects with spring-mass 3d gaussians. In *ECCV*, 2024.

Hongyu Zhou, Jiahao Shao, Lu Xu, Dongfeng Bai, Weichao Qiu, Bingbing Liu, Yue Wang, Andreas Geiger, and Yiyi Liao. Hugs: Holistic urban 3d scene understanding via gaussian splatting. In *CVPR*, 2024a.

Junsheng Zhou, Weiqi Zhang, and Yu-Shen Liu. Diffgs: Functional gaussian splatting diffusion. *NeurIPS*, 2024b.

Xiaoyu Zhou, Zhiwei Lin, Xiaojun Shan, Yongtao Wang, Deqing Sun, and Ming-Hsuan Yang. Drivinggaussian: Composite gaussian splatting for surrounding dynamic autonomous driving scenes. In *CVPR*, 2024c.

A PROOF OF PROPOSITION 1

We construct two distinct parameter sets, $\theta_1 = \{\mathbf{q}_1, \mathbf{s}_1, \mathbf{c}_1, o_1\}$ and $\theta_2 = \{\mathbf{q}_2, \mathbf{s}_2, \mathbf{c}_2, o_2\}$ with $\theta_1 \neq \theta_2$, that generate the identical Single Gaussian Radiance Field (SGRF). The identity $L_{\mathcal{G}_1}(\mathbf{x}, \mathbf{d}) = L_{\mathcal{G}_2}(\mathbf{x}, \mathbf{d})$ for all (\mathbf{x}, \mathbf{d}) requires two conditions to be met:

1. **Geometric Equivalence:** The covariance matrices must be equal, $\Sigma_1 = \Sigma_2$, which implies that the volume densities $\sigma_{\mathcal{G}}(\mathbf{x})$ are identical. We also assume equal opacity, $o_1 = o_2$.
2. **Appearance Equivalence:** The view-dependent color functions must be identical, which requires $\text{SH}(\mathbf{c}_1, \mathbf{R}_1^\top \mathbf{d}) = \text{SH}(\mathbf{c}_2, \mathbf{R}_2^\top \mathbf{d})$ for all $\mathbf{d} \in \mathbb{S}^2$, where \mathbf{R} is the rotation matrix for the quaternion \mathbf{q} .

We construct a distinct parameter set θ_2 by considering a discrete symmetry of the Gaussian ellipsoid. Let $\theta_1 = \{\mathbf{q}_1, \mathbf{s}_1, \mathbf{c}_1, o_1\}$ be an initial parameterization.

Let \mathbf{R}_{flip} be a rotation matrix corresponding to a 180-degree rotation about one of the local axes (e.g., the z-axis), such that $\mathbf{R}_{\text{flip}} = \text{diag}(-1, -1, 1)$. \mathbf{R}_{flip} is its own inverse, $\mathbf{R}_{\text{flip}}^\top = \mathbf{R}_{\text{flip}}$. We define a new parameter set θ_2 as follows:

- Let the new rotation be $\mathbf{R}_2 = \mathbf{R}_1 \mathbf{R}_{\text{flip}}$. This defines a new quaternion $\mathbf{q}_2 \neq \mathbf{q}_1$.
- Let the scales and opacity remain unchanged: $\mathbf{s}_2 = \mathbf{s}_1$ and $o_2 = o_1$.

First, we verify geometric equivalence. The new covariance matrix Σ_2 is:

$$\begin{aligned}\Sigma_2 &= \mathbf{R}_2 \text{diag}(\mathbf{s}_2)^2 \mathbf{R}_2^\top = (\mathbf{R}_1 \mathbf{R}_{\text{flip}}) \text{diag}(\mathbf{s}_1)^2 (\mathbf{R}_1 \mathbf{R}_{\text{flip}})^\top \\ &= \mathbf{R}_1 (\mathbf{R}_{\text{flip}} \text{diag}(\mathbf{s}_1)^2 \mathbf{R}_{\text{flip}}^\top) \mathbf{R}_1^\top\end{aligned}$$

Since \mathbf{R}_{flip} is diagonal, it commutes with the diagonal scaling matrix $\text{diag}(\mathbf{s}_1)^2$, meaning the term in parentheses equals $\text{diag}(\mathbf{s}_1)^2$. Therefore,

$$\Sigma_2 = \mathbf{R}_1 \text{diag}(\mathbf{s}_1)^2 \mathbf{R}_1^\top = \Sigma_1.$$

Geometric equivalence is satisfied.

Next, for appearance equivalence, we must find SH coefficients \mathbf{c}_2 such that:

$$\text{SH}(\mathbf{c}_1, \mathbf{R}_1^\top \mathbf{d}) = \text{SH}(\mathbf{c}_2, (\mathbf{R}_1 \mathbf{R}_{\text{flip}})^\top \mathbf{d}) = \text{SH}(\mathbf{c}_2, \mathbf{R}_{\text{flip}}^\top \mathbf{R}_1^\top \mathbf{d}).$$

Let $\mathbf{v} = \mathbf{R}_1^\top \mathbf{d}$ be the view direction in the local frame of the first Gaussian. The condition becomes $\text{SH}(\mathbf{c}_1, \mathbf{v}) = \text{SH}(\mathbf{c}_2, \mathbf{R}_{\text{flip}}^\top \mathbf{v})$. This states that the function defined by \mathbf{c}_2 when evaluated on a transformed vector must equal the function defined by \mathbf{c}_1 on the original vector. This is equivalent to stating that the function itself has been rotated. The properties of spherical harmonics guarantee that for any rotation, there exists a linear transformation (the Wigner D-matrix \mathbf{D}) that maps the original coefficients to the new ones. We can therefore find \mathbf{c}_2 such that:

$$\mathbf{c}_2 = \mathbf{D}(\mathbf{R}_{\text{flip}}) \mathbf{c}_1.$$

We have constructed a parameter set $\theta_2 = \{\mathbf{q}_2, \mathbf{s}_1, \mathbf{c}_2, o_1\}$, which is distinct from θ_1 (since $\mathbf{q}_2 \neq \mathbf{q}_1$) yet defines the identical radiance field. This discrete symmetry exists for any Gaussian, proving the general proposition.

Furthermore, this non-uniqueness expands from a discrete set to a continuous manifold of solutions for symmetric geometries.

- **Case A (Isotropic):** If $\mathbf{s} = (s, s, s)^\top$, the covariance matrix $\Sigma = s^2 \mathbf{I}$ is invariant under *any* rotation. This gives rise to a continuous, multi-parameter family of equivalent solutions.
- **Case B (Spheroidal):** If two scale components are equal (e.g., $\mathbf{s} = (s_a, s_a, s_b)^\top$), Σ is invariant to any rotation around the local axis of symmetry, resulting in a one-parameter continuous family of redundant solutions.

In all such cases, a corresponding transformation on the SH coefficients preserves appearance equivalence. Since non-unique parameterizations exist in all cases, the proposition is proven.

B PROOF OF UNIQUENESS OF THE REPRESENTATION $\mathcal{E}_i = (\mathcal{M}_i, F_i)$

Assume $\phi_{\mathcal{G}_1} = \phi_{\mathcal{G}_2}$, namely, $\rho_{\mathcal{G}_1}(\mathbf{x}) = \rho_{\mathcal{G}_2}(\mathbf{x}), \forall \mathbf{x} \in \mathbb{R}^3$ and $c_{\mathcal{G}_1}(\mathbf{d}) = c_{\mathcal{G}_2}(\mathbf{d}), \forall \mathbf{d} \in \mathbb{S}^2$. We show this leads to $\mathcal{E}_1 = \mathcal{E}_2$ for two SGRFs. This implies both $\mathcal{M}_1 = \mathcal{M}_2$ and $F_1 = F_2$.

The volume densities are equal:

$$\exp\left(-\frac{1}{2}(\mathbf{x} - \boldsymbol{\mu}_1)^\top \boldsymbol{\Sigma}_1^{-1}(\mathbf{x} - \boldsymbol{\mu}_1)\right) = \exp\left(-\frac{1}{2}(\mathbf{x} - \boldsymbol{\mu}_2)^\top \boldsymbol{\Sigma}_2^{-1}(\mathbf{x} - \boldsymbol{\mu}_2)\right)$$

Taking the natural logarithm of both sides yields that the quadratic forms are identical for all \mathbf{x} :

$$(\mathbf{x} - \boldsymbol{\mu}_1)^\top \boldsymbol{\Sigma}_1^{-1}(\mathbf{x} - \boldsymbol{\mu}_1) = (\mathbf{x} - \boldsymbol{\mu}_2)^\top \boldsymbol{\Sigma}_2^{-1}(\mathbf{x} - \boldsymbol{\mu}_2)$$

An unnormalized Gaussian distribution is uniquely defined by its mean and covariance. Therefore, this equality implies $\boldsymbol{\mu}_1 = \boldsymbol{\mu}_2$ and $\boldsymbol{\Sigma}_1 = \boldsymbol{\Sigma}_2$.

The submanifold \mathcal{M}_i is defined as the level set:

$$\mathcal{M}_i = \{\mathbf{x} \in \mathbb{R}^3 \mid (\mathbf{x} - \boldsymbol{\mu}_i)^\top \boldsymbol{\Sigma}_i^{-1}(\mathbf{x} - \boldsymbol{\mu}_i) = r^2\}$$

Since the parameters $(\boldsymbol{\mu}_i, \boldsymbol{\Sigma}_i)$ that define the level set are identical for both primitives, the resulting sets of points must also be identical. Thus, $\mathcal{M}_1 = \mathcal{M}_2$.

The submanifold color field F_i is defined for a point $\mathbf{x} \in \mathcal{M}_i$ as:

$$F_i(\mathbf{x}) = c_{\mathcal{G}_i}(\mathbf{d}_x), \quad \text{where } \mathbf{d}_x = (\mathbf{x} - \boldsymbol{\mu}_i) / \|\mathbf{x} - \boldsymbol{\mu}_i\|$$

From the hypothesis, we know that $c_{\mathcal{G}_1}(\mathbf{d}) = c_{\mathcal{G}_2}(\mathbf{d})$ holds for any unit direction vector $\mathbf{d} \in \mathbb{S}^2$.

For any point \mathbf{x} on the common manifold $\mathcal{M} = \mathcal{M}_1 = \mathcal{M}_2$, its corresponding direction vector \mathbf{d}_x is an element of \mathbb{S}^2 . We can therefore apply the hypothesis for this specific direction:

$$c_{\mathcal{G}_1}(\mathbf{d}_x) = c_{\mathcal{G}_2}(\mathbf{d}_x)$$

By the definition of F_i , this directly implies:

$$F_1(\mathbf{x}) = F_2(\mathbf{x})$$

This holds for all $\mathbf{x} \in \mathcal{M}$. Thus, the color fields F_1 and F_2 are identical.

C IMPLEMENTATION DETAILS

C.1 SUBMANIFOLD FIELD VAE

For completeness, we note a few aspects not detailed in the main text. Also see Alg. 1 for steps in one training step.

Uniform Point Sampling. The submanifold field \mathcal{E}_i is discretized by using a uniform mesh grid of size (n, n) to sample $P = n^2$ points on the ellipsoidal surface \mathcal{M}_i with respect to area, forming $\mathcal{P}_i = \{(\mathbf{x}_{i,k}, F_i(\mathbf{x}_{i,k}), \alpha_i)\}_{k=1}^P$.

Decoding Gaussian Parameters. After decoding, we recover Gaussian parameters from the reconstructed point cloud by first applying batched PCA to estimate the ellipsoid axes and orientation: we compute the mean and covariance of the points, perform eigen decomposition to obtain principal axes, and ensure a right-handed coordinate system. The logarithm of the axis lengths gives the scale parameters, and the rotation matrix is converted to a quaternion using a numerically stable batched algorithm. For appearance, we compute ellipsoid-normalized directions for each point and fit spherical harmonics coefficients to the RGB values via regularized batched least-squares. Opacity is estimated by averaging and logit-transforming the per-point values.

Algorithm 1 SF-VAE: one training step for a minibatch of submanifold fields

Require: Batch $\{(\mu_i, \Sigma_i, \mathbf{c}_i, o_i)\}_{i=1}^B$, fixed $r^2=1$, point count P

- 1: **for** each i **do**
- 2: (*Sampling on \mathcal{M}_i*) Sample $\{\mathbf{u}_k\}_{k=1}^P$ quasi-uniformly on \mathbb{S}^2 ; set $\mathbf{x}_{i,k} \leftarrow \mu_i + \Sigma_i^{1/2} \mathbf{u}_k$ so that $(\mathbf{x}_{i,k} - \mu_i)^\top \Sigma_i^{-1} (\mathbf{x}_{i,k} - \mu_i) = r^2$
- 3: (*Color-opacity*) $\mathbf{d}_{i,k} \leftarrow (\mathbf{x}_{i,k} - \mu_i) / \|\mathbf{x}_{i,k} - \mu_i\|$; $\mathbf{c}_{i,k} \leftarrow \text{SH}(\mathbf{c}_i, \mathbf{d}_{i,k})$; $\alpha_{i,k} \leftarrow \sigma(o_i)$
- 4: (*Point set*) $\mathcal{P}_i \leftarrow \{(\mathbf{x}_{i,k}, \mathbf{c}_{i,k}, \alpha_{i,k})\}_{k=1}^P$
- 5: **end for**
- 6: (*Encode*) $(\mu_i^z, \log \sigma_i^{2,z}) \leftarrow E(\mathcal{P}_i)$; $\mathbf{z}_i \leftarrow \mu_i^z + \sigma_i^z \odot \varepsilon$, $\varepsilon \sim \mathcal{N}(0, I)$
- 7: (*Decode*) $(\widehat{\mathcal{M}}_i, \widehat{F}_i, \widehat{\alpha}_i) \leftarrow D(\mathbf{z}_i)$; $\widehat{\mathcal{P}}_i \leftarrow \{(\widehat{\mathbf{x}}_{i,k}, \widehat{F}_i(\widehat{\mathbf{x}}_{i,k}), \widehat{\alpha}_i)\}$
- 8: (*Recover parameters*) $\widehat{\Sigma}_i \leftarrow \text{PCA}(\{\widehat{\mathbf{x}}_{i,k}\})$; $\widehat{\mathbf{c}}_i \leftarrow \arg \min_{\mathbf{c}} \sum_k \|\text{SH}(\mathbf{c}, \widehat{\mathbf{d}}_{i,k}) - \widehat{F}_i(\widehat{\mathbf{x}}_{i,k})\|_2^2$
- 9: (*Loss*) $\mathcal{L}_{\text{rec}} \leftarrow W_2^{(\varepsilon)}(\mathcal{P}_i, \widehat{\mathcal{P}}_i)$ with $d(\cdot, \cdot)$ from Eq. (8); $\mathcal{L} \leftarrow \mathcal{L}_{\text{rec}} + \beta \cdot \text{KL}$
- 10: (*Update*) $\theta_E, \theta_D \leftarrow \theta_E, \theta_D - \eta \nabla_{\theta_E, \theta_D} \mathcal{L}$

C.2 GENERATED 3D GAUSSIAN PRIMITIVES DATASET

Parameter priors and sampling Each primitive \mathcal{G}_i is sampled as $\theta_i = \{\mu_i, \mathbf{q}_i, \mathbf{s}_i, \mathbf{c}_i, o_i\}$ and converted to $(\mu_i, \Sigma_i, \mathbf{c}_i, \alpha_i)$ with $\Sigma_i = R(\mathbf{q}_i) \text{diag}(\exp(\mathbf{s}_i))^2 R(\mathbf{q}_i)^\top$ and $\alpha_i = \sigma(o_i)$. Unless otherwise stated we use:

- **Mean.** $\mu_i = (0, 0, 0)$. Since our setting only samples single Gaussians, extrinsic information is not needed.
- **Rotation.** \mathbf{q}_i is sampled uniformly on $SO(3)$ (normalized and, if needed, enforce a canonical sign).
- **Scale.** Log-axes $\mathbf{s}_i \in \mathbb{R}^3$ drawn i.i.d. from $\mathcal{U}([s_{\min}, s_{\max}])$; set activated scales $\exp(s_i)$.
- **SH coefficients.** Let $\beta > 1$ be the decay factor (in code, $\beta = 4$). For degree $\ell = 0, \dots, L$, we draw the $(2\ell+1)$ -dimensional SH band as $\mathbf{c}_\ell \sim \mathcal{N}(\mathbf{0}, \sigma_\ell^2 I_{2\ell+1})$, $\sigma_\ell = \beta^{-\ell}$, i.e., $\text{Var}[c_{\ell,m}] = \beta^{-2\ell}$ for $m = -\ell, \dots, \ell$. If coefficients above the chosen degree L are padded up to L_{\max} , we use i.i.d. noise $c_{\ell,m} \sim \mathcal{N}(0, \sigma_{\text{void}}^2)$ with $\sigma_{\text{void}} = 0.05$.
- **Opacity.** Logit $o_i \sim \mathcal{U}([o_{\min}, o_{\max}])$, with $\alpha_i = \sigma(o_i)$.

To sum up, we can describe the data distribution in this dataset as:

$$\begin{aligned} \mathcal{D} = \{(\mu_i, \mathbf{q}_i, \mathbf{s}_i, \mathbf{c}_i, o_i)\}_{i=1}^N &\stackrel{\text{i.i.d.}}{\sim} \underbrace{\delta_{\mathbf{0}}}_{\mu} \times \underbrace{\mathcal{U}(SO(3))}_{\mathbf{q}} \times \underbrace{\mathcal{U}([s_{\min}, s_{\max}])^3}_{\mathbf{s}} \\ &\times \underbrace{\left(\prod_{c \in \{R, G, B\}} \left[\prod_{\ell=0}^L \mathcal{N}(0, \beta^{-2\ell})^{2\ell+1} \times \prod_{\ell=L+1}^{L_{\max}} \mathcal{N}(0, \sigma_{\text{void}}^2)^{2\ell+1} \right] \right)}_{c \in \mathbb{R}^{3 \times K}, K = (L_{\max}+1)^2} \\ &\times \underbrace{\mathcal{U}([o_{\min}, o_{\max}])}_{o}, \quad \beta > 1 \text{ (default 4)}, \sigma_{\text{void}} = 0.05. \end{aligned}$$

where $\beta > 1$ is the SH variance-decay factor (default $\beta=4$) and σ_{void} is the padding noise std (default 0.05). Activations used downstream are $\Sigma_i = R(\mathbf{q}_i) \text{diag}(\exp(\mathbf{s}_i))^2 R(\mathbf{q}_i)^\top$ and $\alpha_i = \sigma(o_i)$.

Defaults and ablations Default hyperparameters: $N=500K$, $L_{\max}=3$ ($K=16$), $P=144$, $s_{\min} = -8$, $s_{\max} = 0$, $o_{\min} = -5$, $o_{\max} = 10$. These parameters are built from statistical analysis of data distribution in diverse 3DGS datasets. We ablate $P \in \{36, 64, 144, 576\}$ in the main paper to assess reconstruction vs. cost.

Data Formatting and Processing. For each of the randomly synthesized primitive we store the native tuple θ_i (float32 arrays for μ , \mathbf{q} , \mathbf{s} , \mathbf{c} , o). The discretized field \mathcal{P}_i is sampled from the primitive of θ_i to a tensor of $(B, P, 7)$ where 7 is $(x, y, z, r, g, b, \alpha)$. It can be obtained at runtime to reduce memory and storage requirements. The dataset exposes toggles to return either θ or \mathcal{P} .

Algorithm 2 GAUSSIANGEN: Generate one colored point cloud from a random Gaussian

Require: point count P (default 144), SH degree L_{\max} with $K = (L_{\max}+1)^2$

- 1: **Sample raw parameters** $\mu \in \mathbb{R}^3$, $\mathbf{s} \in \mathbb{R}^3$, $\mathbf{q} \in SO(3)$, $o \in \mathbb{R}$, $\text{feat_dc} \in \mathbb{R}^3$, $\text{feat_extra} \in \mathbb{R}^{3(K-1)}$
- 2: **Assemble SH coefficients** $\mathbf{C} \in \mathbb{R}^{3 \times K}$ by stacking per channel:

$$\mathbf{C}_r \leftarrow [\text{feat_dc}[0], \text{feat_extra}[0 : (K-1)]]$$

$$\mathbf{C}_g \leftarrow [\text{feat_dc}[1], \text{feat_extra}[(K-1) : 2(K-1)]]$$

$$\mathbf{C}_b \leftarrow [\text{feat_dc}[2], \text{feat_extra}[2(K-1) : 3(K-1)]]$$
- 3: **Activate parameters**

$$\mathbf{q} \leftarrow \mathbf{q}/\|\mathbf{q}\|; R \leftarrow R(\mathbf{q}); \sigma \leftarrow \exp(\mathbf{s}); \alpha \leftarrow \sigma(o)$$
- 4: **Build surface grid**

$$n \leftarrow \sqrt{P};$$
 create angular grids $u \in [0, 2\pi)$ and $v \in [0, \pi]$ of size $n \times n$
 directions $\mathbf{d}(u, v) \in \mathbb{S}^2$ from spherical angles (u, v)
- 5: **Map to ellipsoid (iso-density $r^2=1$)**

$$\mathbf{x}(u, v) \leftarrow \mu + R \text{diag}(\sigma) \mathbf{d}(u, v)$$
- 6: **Evaluate color field**

$$\mathbf{c}(u, v) \leftarrow \text{SH}(\mathbf{C}, \mathbf{d}(u, v))$$

 (optional) color post-process: $\mathbf{c} \leftarrow \text{clip}(\mathbf{c}+0.5, 0, 1)$
- 7: **Pack output**
 replicate α to all points; flatten grids to P points
return $\{(\mathbf{x}_k, \mathbf{c}_k, \alpha)\}_{k=1}^P \in \mathbb{R}^{P \times 7} // (x, y, z, r, g, b, \alpha)$

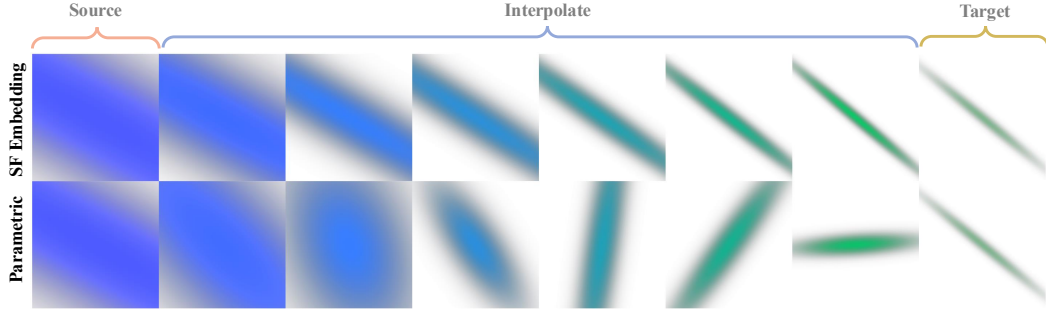
D ADDITIONAL EVALUATION AND VISUALIZATION RESULTS

Figure 7: Sample visual comparison of linear interpolation in submanifold field embedding space and parametric space. Interpolation in SF embedding shows smooth transition from source to target. Perturb \mathbf{s} and \mathbf{q} will dramatically change the geometry of the resulted Gaussian, verifying the feature heterogeneous problem.

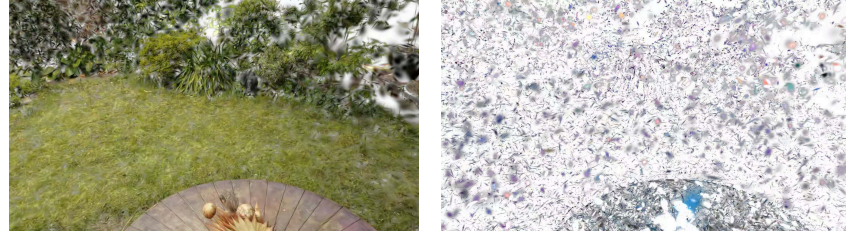


Figure 8: When rotation \mathbf{q} is inverted to $-\mathbf{q}$, the submanifold field model (left) can still correctly reconstruct the scene, while parametric model fails to process this equivalent rotation.



Figure 9: Full qualitative results for rasterization using different model configurations on Mip-NeRF 360.